Presence and Consequences of Coexisting Methane Gas With Hydrate Under Two Phase Water-Hydrate Stability Conditions

Sourav K. Sahoo[1,2] (iD), Héctor Marín-Moreno[1] (iD), Laurence J. North[1], Ismael Falcon-Suarez[1], Bangalore N. Madhusudhan[3], Angus I. Best[1] (iD), and Tim A. Minshull[2] (iD)

[1]National Oceanography Centre, University of Southampton Waterfront Campus, European Way, Southampton, UK, [2]National Oceanography Centre Southampton, University of Southampton, European Way, Southampton, UK, [3]Faculty of Engineering and the Environment, University of Southampton, Southampton, UK

Abstract Methane hydrate saturation estimates from remote geophysical data and borehole logs are needed to assess the role of hydrates in climate change, continental slope stability, and energy resource potential. Here we present laboratory hydrate formation/dissociation experiments in which we determined the methane hydrate content independently from pore pressure and temperature and from electrical resistivity. Using these laboratory experiments, we demonstrate that hydrate formation does not take up all the methane gas or water even if the system is under two phase water-hydrate stability conditions and gas is well distributed in the sample. The experiment started with methane gas and water saturations of 16.5% and 83.5%, respectively; during the experiment, hydrate saturation proceeded up to 26% along with 12% gas and 62% water remaining in the system. The coexistence of hydrate and gas is one possible explanation for discrepancies between estimates of hydrate saturation from electrical and acoustic methods. We suggest that an important mechanism for this coexistence is the formation of a hydrate film enveloping methane gas bubbles, trapping the remaining gas inside.

1. Introduction

Hydrate is a naturally occurring ice-like, crystalline solid comprising a hydrogen-bonded water lattice with trapped gas molecules that forms in seafloor sediments at high pressures and low temperatures (Kvenvolden, 1993). Nearly all the gas in natural hydrates is methane, with the remainder comprising higher order hydrocarbons such as ethane (Kvenvolden, 1993). Remote geophysical methods are used to quantify seafloor methane hydrates over broad areas. Typically, these methods exploit the increase in seismic velocity (e.g., Fohrmann & Pecher, 2012; Lee & Collett, 2006a; Schnurle et al., 2004) and electrical resistivity (e.g., Hsu et al., 2014; Schwalenberg et al., 2010; Weitemeyer et al., 2006) caused when hydrate replaces saline water in sediment pores. However, accurate quantification of methane hydrate saturation is hampered by uncertainties in the relationship between these parameters and hydrate content (e.g., Goswami et al., 2015; Hsu et al., 2014; Lee & Collett, 2008; Schnurle et al., 2004).

Subseabed electrical resistivity can be measured using borehole logging (e.g., Miyakawa et al., 2014) or marine controlled source electromagnetic methods (e.g., Weitemeyer et al., 2006). Some field locations show discrepancies between hydrate saturations derived from resistivity and seismic/sonic methods (Table 1). This difference is a potential source of uncertainty in estimates from geophysical data of the carbon inventory stored in hydrate and in resulting assessments of well stability and methane production from hydrate reservoirs.

Hydrate content is often estimated from the increase in electrical resistivity compared to background sediments with no hydrates (e.g., Hsu et al., 2014; Lee & Collett, 2008; Schwalenberg et al., 2010; Weitemeyer et al., 2006). However, this method does not differentiate between gas and hydrate because both have higher resistivity than conductive pore fluid (e.g., Lee & Collett, 2008). Hereafter, the term gas is used to describe methane that is not stored in hydrate or dissolved in water and may be mobile or immobile. In seismic data, gas and hydrate have been identified from a decrease and increase in *P* wave velocity, respectively (e.g., Fohrmann & Pecher, 2012; Guerin et al., 1999; Lee & Collett, 2006a; Schnurle et al., 2004). Because of their strong effect on *P* wave velocity (White, 1977), the presence of even small amounts of gas can obscure any increase in velocity caused by the presence of hydrate. In this case, estimates of hydrate content based on *P* wave velocity may differ significantly from those based on resistivity.

Table 1

Hydrate Saturations From Resistivity and Seismic/Sonic Methods

Location	Hydrate saturation (%)		References	Comments
	Resistivity	Seismic/sonic		
Good Weather Ridge, Taiwan	15–16	0–10	1, 2	Seismic: broad area
Hikurangi Margin, NZ	~34	~25	3, 4	Maximum
ODP Leg 204, USA			5	
Site 1244	6.5 ± 3.9	10.2 ± 3.7		
Site 1245	7.9 ± 5.5	10.4 ± 5.6		
Site 1247	4.5 ± 2.8	6.1 ± 3.2		
Kumano Basin, Japan	0–80	0–30	6	Parts of well
Nyegga, Norway	38	14–27	7, 8	In chimney
Vestnesa Ridge, Norway	20–30	~11	9, 10	Outside chimney

Note. References: 1, Schnurle et al. (2004); 2, Hsu et al. (2014); 3, Fohrmann and Pecher (2012); 4, Schwalenberg et al. (2010); 5, Lee and Collett (2006a); 6, Miyakawa et al. (2014); 7, Attias et al. (2016); 8, Plaza-Faverola et al. (2010); 9, Goswami et al. (2015); 10, Hustoft et al. (2009).

The presence of coexisting hydrate and gas within the gas hydrate stability zone (GHSZ) has been inferred in several locations away from seabed methane plumes (e.g., Guerin et al., 1999; Milkov et al., 2004; Lee & Collett, 2006a; Miyakawa et al., 2014). Such field studies have attributed this presence of gas within the GHSZ to (i) influx of gas into the GHSZ along fracture/faults (Gorman et al., 2002; Lee & Collett, 2006a; Smith et al., 2014); (ii) local deviations from two phase water-hydrate stability conditions (pressure-temperature [PT]-salinity) resulting in local hydrate dissociation within the GHSZ (Guerin et al., 1999; Milkov et al., 2004); or (iii) hydrate formation kinetics (Torres et al., 2004). Drilling activities may also dissociate hydrates around a well, releasing gas within the GHSZ (Lee & Collett, 2006a).

At Site 1245 of ODP Leg 204, the amount of gas within the GHSZ was inferred independently from NMR logs and sonic velocity logs, with 4 times less gas inferred from sonic logs than from NMR logs (Lee & Collett, 2006a). In the Kumano basin, Nankai Trough, offshore Japan, the presence of coexisting gas within the GHSZ was inferred from velocity and resistivity logs: In certain parts of the well, velocity decreased with no corresponding decrease in resistivity, probably due to the presence of gas (Miyakawa et al., 2014). In both these locations, transport of gas into the GHSZ along faults or local hydrate dissociation during drilling has been inferred (Lee & Collett, 2006a; Miyakawa et al., 2014). Milkov et al. (2004) explained the presence of gas within the GHSZ at Site 1249 of ODP Leg 204 by high residual pore water salinity, which limited further hydrate formation (Hesse & Harrison, 1981; Liu & Flemings, 2006; Milkov et al., 2004). At Site 995 of ODP Leg 164, coexisting gas and hydrate in the base of the GHSZ have been explained by hydrate dissociation in smaller pores because of capillary effects along with hydrate stability in bigger pores (Guerin et al., 1999). Elsewhere, several locations do not show any evidence of coexisting hydrate and gas within the GHSZ (e.g., Fujii et al., 2015).

However, gas can also be present in two phase water-hydrate stability conditions due to two mechanisms. First, hydrate can contain inclusions of gas (Schicks et al., 2006), which could either be connected or disconnected to the pore network. Disconnected inclusions (occlusions) could remain in the hydrate or could also be a prehydrate phase, where hydrate formation is still in process (Schicks et al., 2006). Occlusions of gas may be removed over time by diffusion, but in a dynamic pore fluid system with gas production, diffusion is unlikely to dominate due to its relatively slow rate (Milkov et al., 2004; Suess et al., 2001). Second, hydrate formation can block contacts between gas and water within sediment pores and form pockets of gas (which could include several pores; e.g., Chaouachi et al., 2015; Yang et al., 2016). Kinetic modeling of hydrate formation and dissociation in porous media suggests that it is highly unlikely that hydrate can achieve true equilibrium because there are too many phases in the system (e.g., Vafaei et al., 2014). Therefore, the limiting phase (methane in excess water conditions and water in excess gas conditions) is unlikely to be completely used up to form hydrates even if two phase water-hydrate stability conditions prevail.

Here we present results from a laboratory experiment of methane hydrate formation and dissociation in Berea sandstone. We calculated continuously the evolution of the brine, gas, and hydrate saturations during hydrate formation and dissociation from pore pressure and temperature. Our calculation method does not assume that hydrate formation continues until the limiting phase is exhausted, and we show that about 12% gas coexists with 26% hydrate under pressure, temperature, and salinity conditions favorable for more hydrate formation.

2. Hydrate Formation and Dissociation Experiments

We conducted laboratory experiments involving repeated cycles of methane hydrate formation and dissociation inside a high-pressure cell under excess water conditions.
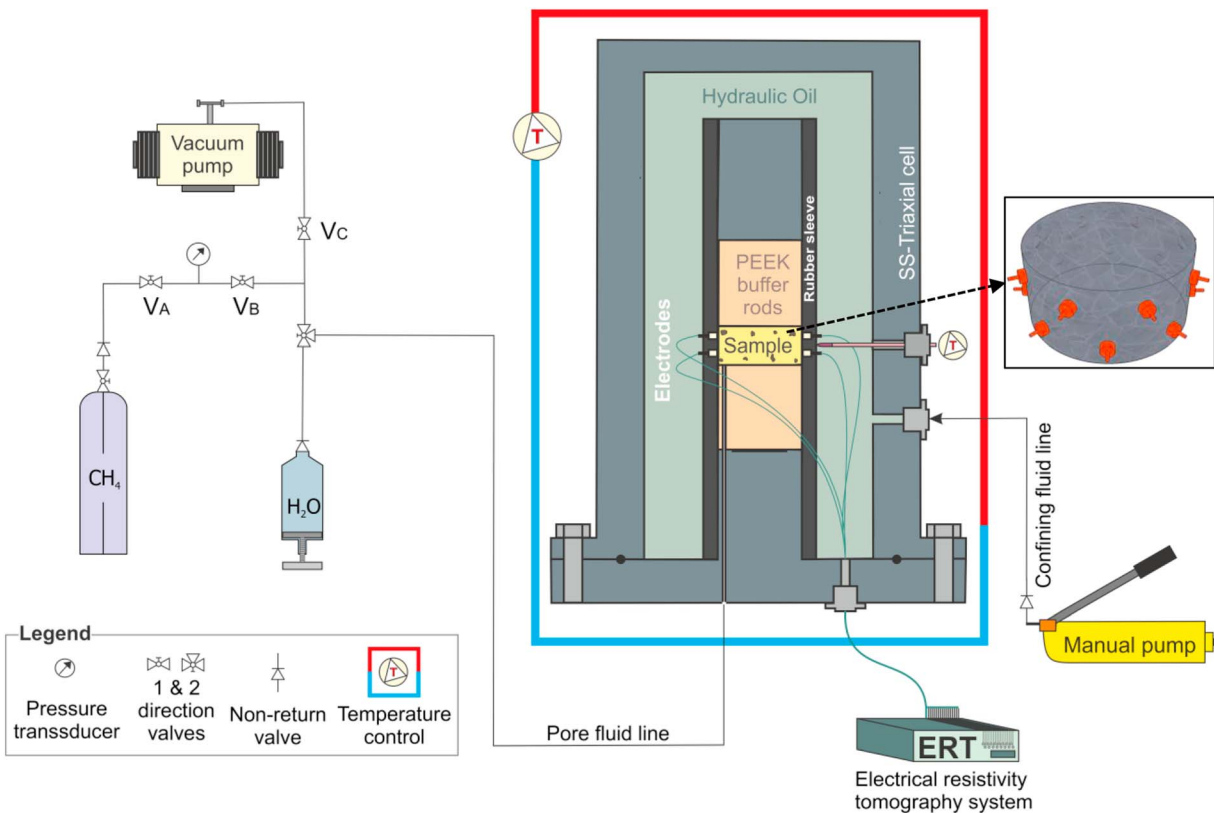
Figure 1. Schematic diagram of the experimental setup, also showing the arrangement of electrodes around the Berea rock sample (5 cm diameter). Scales are approximate.

2.1. Sample Properties and Experimental Setup

For the test, we selected a 2-cm height, 5-cm diameter core sample of Berea sandstone. The porosity was 0.22, and the absolute permeability was 448 mD (~4.5×10^{-13} m^2) at atmospheric conditions. The permeability was measured with (gas) permeameter and the porosity with a pycnometer.

The experiment was conducted in a stainless steel triaxial cell core holder, designed to host and pressurize 5-cm-diameter rock samples up to 65 MPa of confining and pore pressure (Figure 1) and instrumented to monitor temperature (both sample and ambient; M. H. Ellis, 2008). The inner sleeve that prevents the direct contact between the mineral oil used as confining fluid and the rock sample is perforated by 16 electrodes coupled to a data acquisition system. Under typical operating conditions the relative error in resistivity measurement is <0.1% (at frequencies 1–500 Hz) for homogenous and isotropic samples in the electrical resistivity range 1–100 Ω m (North et al., 2013). Axially, perspex buffer rods electrically isolate the sample from the cell. The inner temperature sensor was placed on the outer sidewall of the sleeve at the sample height, to provide accurate monitoring of the sample temperature. The pore fluid pipe line is connected to (i) a pumping-syringe containing a 35-g/L NaCl solution in deionized-deaerated water, (ii) a vacuum pump, and (iii) a CH$_4$-bottle pressurized at 12 MPa (see Figure 1).

2.2. Method of Hydrate Formation

We followed the method of Waite et al. (2004) with an initial brine saturation of 83.5% which allowed an excess water condition (M. H. Ellis, 2008; Priest et al., 2009). Our hydrate formation method and experimental setup represent gas hydrate systems where localized gas reaches the base of the GHSZ.

The sample was first oven-dried at 60°C, placed in the high pressure triaxial cell (Figure 1), then a hydrostatic confining pressure of 10 MPa was applied externally to the sample. A vacuum up to 1 Pa was applied internally to the sample to remove air from the pore space. The presence of air affects the saturation calculation, and some gases present in the air, such as CO$_2$, can also form hydrate. A volume of brine (comprising
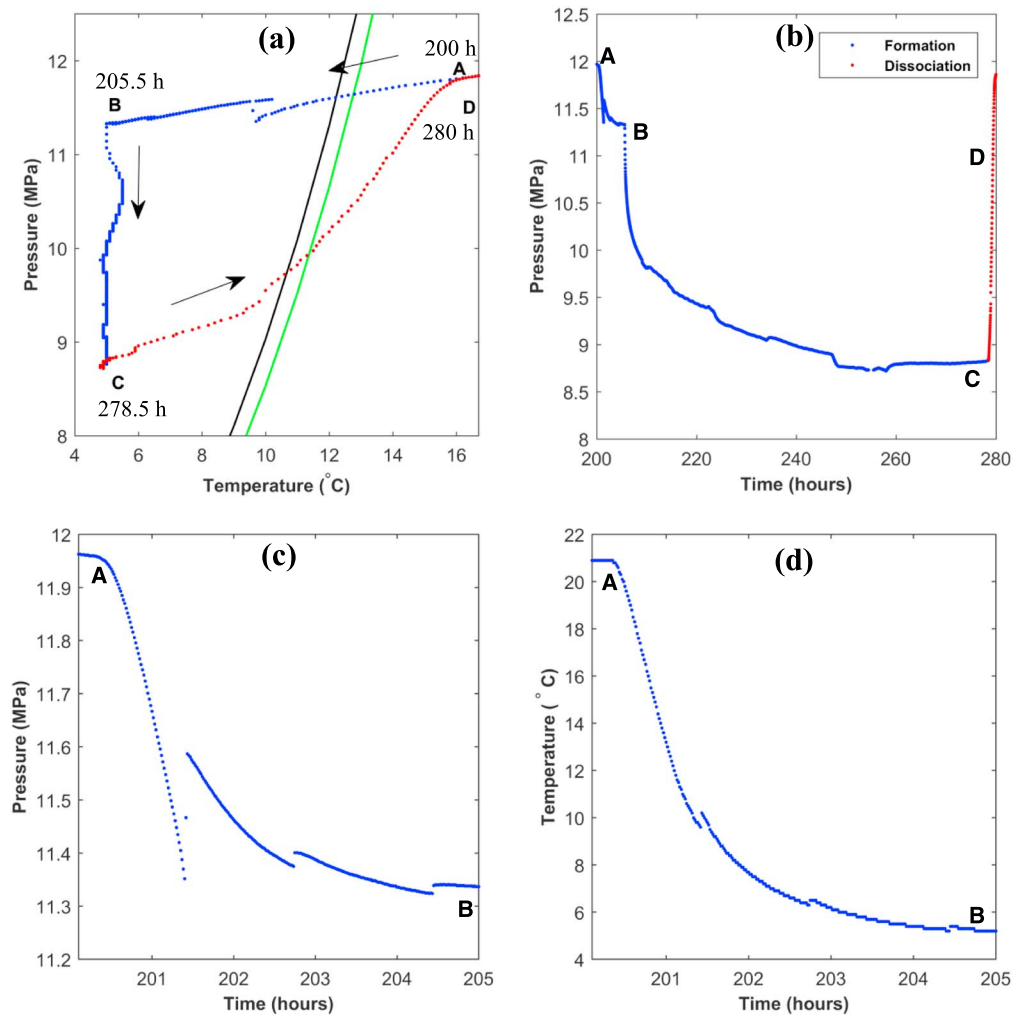
Figure 2. Changes of (a) pressure versus temperature and (b) pressure with time during methane hydrate formation and dissociation in Berea sandstone. Only the second cycle of hydrate formation and dissociation is shown for clarity. The green and black lines are the pure methane hydrate phase boundary for 35 and 46-g/L salinity, respectively, calculated using the approach of Tohidi et al. (1995). The blue dots represent cooling and red dots represent heating. In (a) time is shown in hours (hr). Trajectory ABC marks cooling of the system to 5°C and hydrate formation. Trajectory CD shows hydrate dissociation. (c and d) Pressure and temperature change with time during trajectory AB. See text for further details.

35-g/L NaCl solution in deionized and deaerated water) was injected through the pore fluid line into the Berea rock sample using a syringe pump, calculated to fill 83.5% of the pore space. Hence, the sample was only partially filled with brine, with the remaining pore space available for subsequent methane gas injection (e.g., Waite et al., 2004; Winters et al., 2004). We left the sample for 3 days so that the pore fluids could redistribute throughout the sample by capillary forces. The remaining pore space (16.5%), which was previously under vacuum, may have been occupied by water vapor and/or remaining air.

Methane gas was then injected to achieve a pore fluid pressure of 11.9 MPa (Figure 2), and simultaneously, the confining pressure was increased to 21.9 MPa to maintain a constant differential pressure of 10 MPa during the whole experiment. The pore fluid system was sealed, keeping the reservoir between the sample and valve V_A (Figure 1) filled with methane gas, which is free to move in and out of the sample as a result of potential pore pressure variations. Finally, four cycles of hydrate formation/dissociation were triggered by cooling/heating the setup in a controlled manner, that is, in and out from the gas hydrate stability conditions (GHSC).

The cooling of the system into the GHSC, to a set temperature of 5°C, generated a reduction in pore pressure (Figure 2) that can be explained mainly by hydrate formation, with some contribution from methane gas contraction and increased gas solubility. The pressure reduction appears to take place in two stages
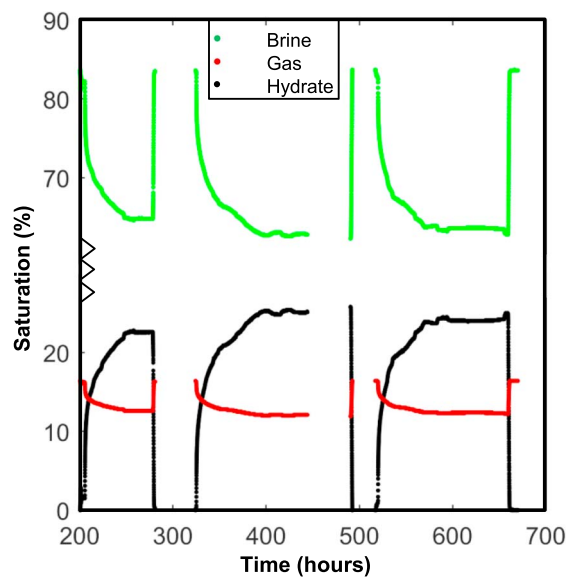
Figure 3. Evolution of water, methane gas, and methane hydrate saturation during three hydrate formation and dissociation cycles in Berea sandstone. The saturations were calculated from the changes in pore pressure and temperature (section 3.1). We used a hydration number of 6.39 corresponding to 90% cage occupancy (Sloan & Koh, 2007). Note the contracted *y* axis scale. The first cycle is not shown because the pressure logger malfunctioned. Relative error in saturation is less than 0.5%.

(Figure 2). On trajectory A-B the system is cooled rapidly (in 5.5 hr). Here the pressure drops due both to cooling and to hydrate formation. On trajectory B-C the temperature remains around 5°C and only the pressure drops. Here the pressure drop is mainly due to hydrate formation and takes much longer (73 he) than on trajectory A-B. The formation of hydrate also generates a slight increase in temperature caused by exothermic hydrate formation (Hwang et al., 1990). This increase is very clear on trajectory B-C. On trajectory A-B, at around 201.4 hr, there is a sudden pore fluid pressure and temperature increase (Figure 2). This pressure increase is likely due to the interplay between the cooling of the system and the exothermic effect of hydrate formation. Cooling and the consumption of pore fluids due to hydrate formation both lead to a decrease in pressure. However, hydrate formation also leads to an increase in temperature, which can result in a slight increase in pressure (Figures 2c and 2d). The net effect depends on the balance between the rate of cooling and the rate of hydrate formation. Once hydrate formation ceased, indicated by the end of the pore pressure decrease (point C in Figure 2), the system was left at that pressure and temperature for several hours to ensure maximum hydrate formation, evidenced by the horizontal asymptotic behavior of the pore pressure (Figure 2b) and of the saturation lines for each cycle (Figure 3).

Hydrate dissociation was initiated by increasing the temperature above the GHSC to room temperature. We also did a separate experiment under identical conditions in which we left the sample under hydrate stability conditions at 5°C (point C in Figure 2a) for 1 month and saw that maximum saturation of methane hydrate occurred in the first 75 hr. This experiment also resulted in 22% hydrate saturation. The differential pressure was held at 10 MPa in the first and second cycles of hydrate formation and dissociation, and then increased to 55 MPa for the third and fourth cycles. This was done to explore the effects of microcracks on acoustic properties (included in future work) that are generally open at lower differential pressures (10 MPa) and closed at higher pressures (55 MPa), based on previous resistivity and ultrasound data for Berea (Han et al., 2011). The initial pore fluid pressure for the third cycle was 11.98 MPa (0.08 MPa above that for the first cycle).

3. Saturation Calculations

We tracked the evolution of the saturations of gas, brine, and hydrate from the changes in pore fluid pressure and temperature using the real gas equation (the PT method), and independently from electrical resistivity measurements (the electrical resistivity tomography [ERT] method).

3.1. PT Method

We calculated continuously the saturations of the three phases (gas, brine, and hydrate) from the changes in pore fluid pressure and temperature using the real gas equation. These measurements were recorded at 1-min intervals during the experiment. This method does not assume that hydrate formation continues until the limiting phase is exhausted (e.g., Sultaniya et al., 2015) nor that coexistence occurs only under three-phase stability conditions (e.g., You et al., 2015). This allows us to deduce the physical processes that occur throughout the cycle of hydrate formation and dissociation.

Our method assumes a closed system and conservation of the molar mass of methane and water in the sample pore space. Methane can be present in hydrate, dissolved in brine, or as gas. Water can be present as liquid in the pore space (brine) or in hydrate (pure water). The pore volume in the sample and inner volume of the input gas pipe were measured before starting the experiment and were assumed to remain constant throughout the experiment. A change in effective pressure can change the sample's pore volume, but for the magnitude of the dynamic stresses applied, this change is negligible (<0.3% for Berea sandstone; Rutter & Glover, 2012). A change in temperature can also change the sample's pore volume. Such changes are likely to be negligible in our experimental range (5–22°C) as the volumetric thermal expansion coefficient of

sandstone is about 3×10^{-5} per °C in the temperature range 20–100°C (Skinner, 1966). So we assumed that the volume of the input gas pipe remains constant because it is always at ambient pressure and the ambient temperature was controlled to 20 ± 2°C. The pores of the Berea sandstone can be occupied by gas, water, or hydrate. Hydrate can only form in the pore space of the sample and no hydrate forms in the gas input pipe because it is outside hydrate stability conditions.

The nonideal gas law is

$$p\,V = n\,R\,T\,Z \tag{1}$$

where p is gas pressure, V is volume, n is the number of moles of methane gas, R is the universal gas constant, and T is temperature. Z is an empirical compressibility factor calculated using the Peng-Robinson equation of state (Peng & Robinson, 1976) and varies with temperature and pressure. Initially, there was no hydrate in the sample. The sample pore volume V_{ts} was independently measured with a pycnometer, and a known volume of water V_{w0}, measured using a syringe pump, was injected into the sample. The initial number of moles of water is given by

$$n_{w0} = \frac{V_{w0}D_{w0}}{M_w} \tag{2}$$

where D_{w0} is the density of brine at 35-g/L salinity and M_w is the molar mass of this brine. For the pipe, from equation (1) we have

$$p_0\,V_p = n_{p0}R\,T_{p0}\,Z_{p0} \tag{3}$$

where p_0 is initial gas pressure, which is the same in both the sample and the pipe, V_p is the volume inside the pipe, n_{p0} is the initial number of moles of methane gas in the pipe, T_{p0} is the temperature in the pipe, and Z_{p0} is the compressibility factor of methane under the initial pipe P-T conditions.

For the sample, equation (1) gives

$$p_0\,V_{ms0} = n_{s0}R\,T_{s0}\,Z_{s0}, \tag{4}$$

$$V_{ms0} = V_{ts} - V_{w0}, \tag{5}$$

where V_{ms0} is the initial volume of methane gas in the sample, n_{s0} is the initial number of moles of methane gas in the sample, T_{s0} is the initial temperature of the sample, and Z_{s0} is the compressibility factor of methane under the initial sample P-T conditions. In our method, we accounted for the dependency of methane solubility in water, denoted by b, on temperature and salinity (Tishchenko et al., 2005) and that of hydrate and brine densities on pressure and temperature (Lu & Sultan, 2008; Millero et al., 1980) using the equation:

$$n_{sw0} = V_{w0}\,D_{w0}\,b_0, \tag{6}$$

where n_{sw0} is the initial number of moles of methane in solution and b_0 is the initial solubility. The total number of moles of methane in the system n_t was therefore

$$n_t = n_{p0} + n_{s0} + n_{sw0}. \tag{7}$$

Once the temperature decreases below that for hydrate stability, hydrate starts to form from the methane and water in the sample's pore space. This process reduces the sample's gas pressure, generating an inflow of methane gas from the pipe to regain equilibrium of pore fluid pressure. The net result is an overall decrease in the gas pressure. From this new gas pressure and the pipe and sample temperatures, T_p and T_s, we can calculate the number of methane moles in each phase. For a gas pressure p

$$V_h = n_h\,\frac{M_h}{D_h}, \tag{8}$$

$$V_w = (n_{w0} - n_h \cdot c)\,\frac{M_w}{D_w}, \tag{9}$$

Table 2
Parameters Used in the Pressure-Temperature Method

Description	Symbol[a]
Number of moles of methane hydrate	n_h
Saturation of methane hydrate	S_h
Pore fluid pressure	p
Total pore space in the sample	V_{ts}
Volume of methane gas in the sample	V_{ms}
Volume of liquid water in the sample	V_w
Volume of hydrate in the sample	V_h
Volume of pipe	V_p
Total number of moles of methane in the system	n_t
Number of moles of methane gas in pipe	n_p
Number of moles of methane gas in sample	n_s
Number of moles of methane in solution	n_{sw}
Number of moles of water in liquid phase	n_w
Temperature in the pipe	T_p
Temperature in the sample	T_s
Compressibility of methane gas in the pipe	Z_p
Compressibility of methane gas in the sample	Z_s
Density of brine	D_w
Density of hydrate	D_h
Solubility of methane	b

[a]Initial values for these parameters are denoted in the text with a subscript 0.

$$V_{ms} = V_{ts} - V_w - V_h, \tag{10}$$

$$p V_p = n_p R T_p Z_p, \tag{11}$$

$$p V_{ms} = n_s R T_s Z_s, \tag{12}$$

$$n_{sw} = V_w D_w b, \tag{13}$$

where V_h is the volume of hydrate, n_h is the number of moles of hydrate, M_h is the molecular mass of hydrate, D_h is the density of hydrate, and c is the hydration number (i.e., the number of water molecules required to form hydrate per molecule of methane). The total number of moles of methane in the system remains constant, so n_h can be obtained from

$$n_h = n_t - n_p - n_s - n_{sw}. \tag{14}$$

The hydrate saturation is given by

$$S_h = \frac{V_h}{V_{ts}}. \tag{15}$$

Combining equations (8)–(15), we obtain

$$S_h = \frac{\left(\frac{p_0 V_{p0}}{R T_{p0} Z_{p0}} + \frac{p_0 (V_{ts} - V_{w0})}{R T_{s0} Z_{s0}} + V_{w0} D_{w0} b_0 - \frac{p V_p}{R T_p Z_p} - \frac{p V_s}{R T_s Z_s} - V_w D_w b \right) \frac{M_h}{D_h}}{V_{ts}}. \tag{16}$$

All the symbols defined in this section are listed in Table 2, and constants are listed in Table 3.

3.2. ERT Method

We estimated the saturation of resistive material in the pore space from measured bulk resistivity of the sample. As both hydrate and gas are resistive compared to the conductive brine, it is not possible to obtain the individual saturations of gas and hydrate separately by this approach.

To determine this saturation, the first step is to calculate the saturation of brine. Several approaches can be used to estimate the saturation of brine from measured electrical resistivity (e.g., Archie, 1942; Bussian, 1983; de Lima & Sharma, 1990; Glover, 2010; Revil et al., 1998; Simandoux, 1963; Waxman & Smits, 1968). This interpretation is complicated in the presence of clay minerals as they have charge deficiency. The "counter ions" required to balance this charge deficiency are in the double layer. These counter ions can move along the grain water surface under the influence of an external electric field. Hence, the macroscopic electrical conduction in a saturated/partially saturated porous medium with clay can be via (a) bulk conduction caused by the movement of ions of the conducting pore fluid and (b) surface conduction in the vicinity of the fluid/grain interface (e.g., Bussian, 1983; Revil & Glover, 1998; Waxman & Smits, 1968). A wide variety of formulations have been developed to account for both surface and bulk conduction. The earlier models described the effect of surface conduction in terms of the volume of shale, while more recent models attempt to account for the physics of the diffuse ion double layer surrounding clay particles (e.g., Clavier et al., 1984; Revil et al., 1998; Simandoux, 1963; Waxman & Smits, 1968). We choose to use the Waxman-Smits formula for partial brine saturation (Waxman & Smits, 1968).

Table 3
Constants Used in the Pressure-Temperature Method

Description	Symbol	Values
Ratio of water to methane in hydrate (Sloan & Koh, 2007)	c	6.39
Molar mass of brine (35 g/L)	M_w	0.0186 Kg
Molar mass of hydrate (structure I)	M_h	0.1312 Kg
Universal gas constant	R	8.314 Jmol^{-1} K^{-1}

$$S_w = \left(\frac{\Phi^{-m} \rho_w}{\rho_t (1 + \rho_w B Q_v / S_w)} \right)^{\frac{1}{n}}, \tag{17}$$

$$B = 4.6 \left(1 - 0.6 e^{-\frac{1}{1.3 \rho_w}} \right), \tag{18}$$

$$Q_v = \frac{CEC(1 - \Phi)D_O}{\Phi},$$ (19)

where S_w is brine saturation, ρ_t is the measured sample resistivity, ρ_w is brine resistivity, and Φ is porosity. Q_v is the concentration of clay exchange cations or counter ions per unit pore volume of the rock and should be measured ideally in the laboratory by analyzing several samples with different brine saturations (Waxman & Smits, 1968). B represents the average mobility of the counter ions near the grain surfaces, CEC is the cation exchange capacity, and D_o is mineral grain density. The empirical parameters m and n are the cementation coefficient and the saturation exponent, respectively.

Zhan et al. (2010) showed experimentally for a similar porosity Berea sandstone (22.98–23.60%) that the Waxman-Smits model gives reliable results for our salinity (Figure 6 of Zhan et al., 2010). Glover et al. (1994) presented laboratory data on the variation of Berea sandstone conductivity with fluid conductivity. They showed that, for low pore fluid conductivity (<0.001 S/m), bulk conductivity is independent of pore fluid conductivity and tends to be constant. For higher pore fluid conductivity (<1 S/m), the saturated rock conductivity is controlled mainly by the movement of ions through the bulk fluid and seems to be independent of any surface conduction effect. As we used brine of 35 g/L (measured conductivity at 25°C temperature is 5.2 S/m), we are in the higher pore fluid conductivity zone where surface conduction effects have only a small effect on bulk rock conductivity. The experiments of Glover et al. (1994) and Zhan et al. (2010) had no hydrate, but hydrate is resistive compared to saline pore fluid and has negligible surface conduction (e.g., Lee & Collett, 2006b; Spangenberg, 2001). Several studies have shown that surface conduction contributes substantially to the macroscopic conductivity at low salinity and/or high temperature, even in low clay content sandstone (Bussian, 1983; Revil & Glover, 1998; Waxman & Smits, 1968). Since our sample has a low clay content of 2.3% by weight (X-ray powder diffraction analysis; Han et al., 2015), the pore fluid has a high salinity (35-gm/L NaCl with conductivity of 5.22 S/m at 25°C), and the temperature is low (5°C), we conclude that the Waxman-Smits model should be applicable in our case.

As natural hydrate can be found also in clay rich sediments, appropriate clay conduction models should be used in such studies. We used the Waxman-Smits model, but several modifications, refinements, or other models exist. For example, Clavier et al. (1984) proposed the dual water model, a modified form of the Waxman-Smits model with two types of pore water, of which only one is affected by surface conduction. Kan and Sen (1987) modeled clays as periodic arrays of charged insulating cylinders or spheres, immersed in symmetrical monovalent electrolyte. Revil and Glover (1998) discussed the theoretical framework of surface conduction predictions. Revil et al. (1998) accounted for the difference in behavior of anions and cations. de Lima and Sharma (1990) discussed a model based on shape and occurrence of clay, such as clay coating the sand grains or as individual clay grains. For a more detail review on conductivity models refer to, for example, Glover (2010), de Lima and Sharma (1990), and Mavko et al. (1998).

The resistivity of brine is temperature-dependent, and we calibrated it using the following expression (e.g., McCleskey et al., 2012):

$$\rho_w = \frac{\rho_{25}}{1 + \alpha(T - 25)},$$ (20)

where T (°C) is temperature, α is the temperature compensation factor, and ρ_{25} (Ωm) is the resistivity of brine at 25°C. Values of ρ_{25} were measured using a conductivity meter with $\alpha = 1.9\%$, similar to other studies (e.g., McCleskey et al., 2012). For a mixture of sand and clay, the CEC can be calculated from

$$CEC = m_c \sum \chi_i CEC_i,$$ (21)

where m_c is the mass fraction of clay minerals in the whole rock, χ_i is the relative volume fraction of each clay mineral, and CEC_i is the cation exchange capacity of each clay mineral. The cation exchange capacity of quartz can be neglected due to its large size (hence small amount of surface change per unit mass) in comparison to clay minerals (D. V. Ellis & Singer, 2007).

This method of calculating CEC assumes a mixture of sand and clay and does not account for the various clay morphologies (e.g., clay as cement or grains) in Berea sandstone. We used 0.09-meq/g CEC for authigenic illite (Thomas, 1976). A value of 2 was used for n (Waxman & Smits, 1968). The value of m was determined by fitting the initial resistivity for the known initial brine saturation, found to be 2.825, which is within the

range of 1.3 to 4 reported by Jackson et al. (1978). As hydrate forms, the value of m increases (Chen et al., 2008; Spangenberg, 2001), but the exact form of this increase is not known. To account for this change, we arbitrarily assumed a slightly higher value of m = 3.1 for hydrate saturations above 5% (Chen et al., 2008; Spangenberg, 2001). Spangenberg (2001) modeled the variation of n with water saturation, during hydrate formation. He showed that n increases significantly only for water saturation below 40% and n is almost constant for water saturation above 40%. In our experiment water saturation started from 83.5% and decreased up to 62% with hydrate formation; hence, we did not vary the value of n.

4. Results and Discussion

4.1. Three Phase Coexistence

The results of the PT method provide evidence for the coexistence of methane gas, methane hydrate, and brine in our experiments. When the pressure and temperature reached stability conditions, methane hydrate nucleation and growth started, followed by an increase in hydrate saturation and a decrease in gas and brine saturation (Figure 3). Even though we allowed enough time (80–180 hr) for hydrate formation to continue (see section 2 for further details), and there was always stoichiometrically sufficient methane gas and brine available for more methane hydrate formation, the reaction stabilized at a maximum methane hydrate saturation between 23 and 26% and methane gas saturation between 12 and 13% of the pore space (Figure 3). The maximum relative error in saturation calculated using the PT method is less than 0.5%. This phenomenon was observed also in two additional cycles of methane hydrate formation and dissociation, indicating the coexistence of three phases (gas, brine, and hydrate) with similar maximum methane hydrate and methane gas saturations and an asymptotic behavior of the saturation curves during hydrate formation in each cycle (Figure 3). At the maximum hydrate saturation, application of small perturbations in the confining pressure could have ruptured hydrate shells, trapping gas, and allowed further hydrate formation (Fu et al., 2017). Such perturbations were not applied, so our estimate of coexisting gas may represent an upper bound for our experimental setup.

Methane hydrate is a nonstoichiometric solid with variable cage occupancy (Sloan & Koh, 2007). We used a hydration number of 6.39, corresponding to 90% cage occupancy (Sloan & Koh, 2007) for the calculation shown in Figure 3. If the cage occupancy is 100%, c is 5.75 (Sloan & Koh, 2007) and the resulting maximum hydrate saturation decreases by 2%.

In section 1, we listed several mechanisms allowing three phase coexistence of methane gas with hydrate. Here we discuss some of the mechanisms that are relevant to our experimental study. Methane hydrate may form when methane gas and water are in contact and have conditions favorable for hydrate formation. Our experimental pressure and temperature conditions of 8.8 MPa and 5°C were well within the hydrate stability field for 35-g/L brine, but the salinity of the remaining pore water increases due to hydrate formation. Our experiments started with 35-g/L salinity, and a 26% hydrate saturation would have increased the mean salinity to about 46 g/L. At this salinity, our experimental pressure and temperature conditions are still within the GHSC (Figure 2a), as calculated using the approach of Tohidi et al. (1995). This calculation does not consider the effect of porous medium properties such as pore size, surface structure, and mineral composition that can all affect the GHSC (e.g., Clennell et al., 1999; Handa & Stupin, 1992; Henry et al., 1999). Some experimental results suggest that surface structure and mineral composition may have little effect on GHSC (Riestenberg et al., 2003), while capillary effects due to pore size can be important (Clennell et al., 1999; Uchida et al., 2004). Therefore, we consider only capillary effects.

Clennell et al. (1999) argued that methane hydrate behavior can be analogous to that of ice, as also suggested by other authors (e.g., Handa & Stupin, 1992). The freezing point of ice is lower in a fine-grained porous medium, such as soil, than in bigger pores, such as in sand. This is due to curved water-ice interfaces that increase the free energy of pore water (Everett, 1961). In small pores, the curvature is high and the excess free energy is also high. In big pores, the curvature is low, and so is the excess free energy. Clennell et al. (1999) calculated the decrease in the freezing point of ice inside a pore relative to the bulk freezing point (in a pore of infinite pore radius) and extrapolated that to methane hydrate. We rearranged equation (8) of Clennell et al. (1999) to calculate the minimum pore radius for which hydrate can form under our experimental conditions of 8.8 MPa and 5°C.
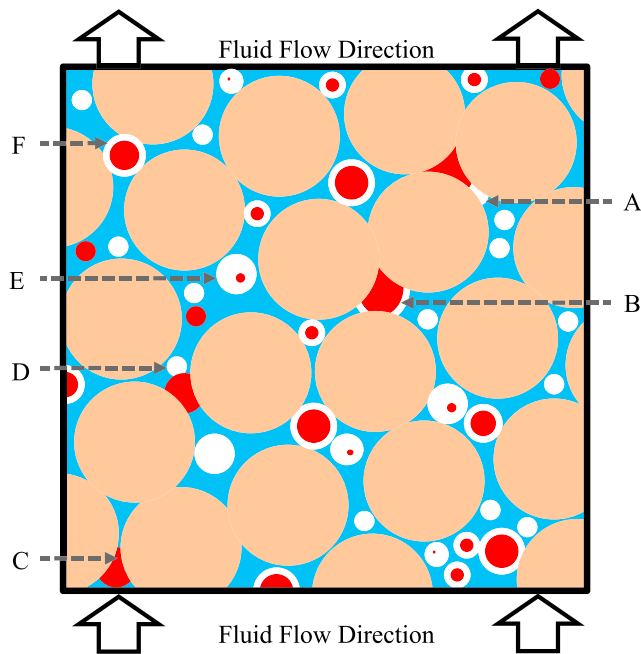
Figure 4. Conceptual model showing various mechanisms (marked A to F) for coexistence of methane gas and hydrate even when methane hydrate stability conditions prevail in the system. The red color is methane gas, white is hydrate, brown is sand, and blue is saline water (brine). (a and b) Pore blocked by hydrate formation. (c) Capillary pressure of pore not allowing the gas to move through it. (d) Capillary pressure of the pore increased by hydrate formation, not allowing further passage of gas. (e) Occlusions (unconnected inclusions) of gas within hydrate. (f) Hydrate film enveloping the gas bubble.

$$r_e = \frac{2\gamma_{iw} T_{i,\text{bulk}} \cos\theta_{iw}}{\rho_w \Delta H_{f,i} \Delta T_{i,\text{pore}}}, \qquad (22)$$

where r_e is the radius of the pores, γ_{iw} is the specific surface energy between ice and water, $T_{i,\text{bulk}}$ is the absolute melting temperature of ice (without considering pore radius effects), θ_{iw} is the wetting angle, ρ_w is the density of water, $\Delta H_{f,\ i}$ is the specific enthalpy of formation of ice, and $\Delta T_{i,\text{pore}}$ is the change in melting temperature due to pore size effects. For our experimental pressure of 8.8 MPa, the hydrate-water phase boundary temperature ($T_{i,\text{bulk}}$) is 9.8 °C (calculated using the approach of Tohidi et al., 1995), and therefore, $\Delta T_{i,\text{pore}}$ is −4.8°C, giving a minimum pore radius of 9.5 nm for $\gamma_{iw} = 26.7$ mJ m^{-2}, $\theta_{iw} = 180°$, $\rho_w = 1,000$ kg m^{-3}, and $\Delta H_{f,\ i} = 333$ kJ Kg^{-1} (Clennell et al., 1999).

We also measured the pore size distribution using X-ray computed tomography at the Swiss Light Source at the Paul Scherrer Institute. The optical objective used for imaging was 20×, which provided 325-nm voxel resolution. The pore size varied from 11.39 to 73.11 μm, so capillary effects in our sample should not have limited the formation of hydrate. Note that only a small part (7.27 mm diameter and 8 mm high) of the sample was studied in the CT scan, and we assumed that the observed pore size distribution is representative of the whole sample. Clennell et al.'s (1999) equation is for pure water, while our pore fluid had an average salinity of up to 46 g/L at maximum hydrate saturation. Sun and Duan (2007) developed a thermodynamic model for the effect of pore size and salinity on hydrate stability. We used their open online calculator (models.kl-edi.ac.cn/models.htm) and found a minimum pore radius of less than 3.2 nm, confirming the minor effect of pore size for our experimental conditions. We note also that it is very unlikely that hydrate formation can reduce the effective pore size to values close to the minimum pore radius because that could only happen when the pore is almost completely occupied by hydrate.

When hydrate forms, it can create a physical barrier between methane gas and water that prevents further hydrate formation. This physical barrier can be of various types:

1. Hydrate may form and dissociate only near the inlet pipe if the methane gas/brine is not distributed in the sample. This scenario is highly unlikely because the sample was vacuumed and then 83% of the pore space was filled with brine. These conditions were kept for 3 days, allowing the brine to spread within the sample. The gas would also be distributed within the sample before hydrate forms because (i) the inlet pipe is on the lower surface of the sample, and methane gas would likely move upward due to buoyancy, and (ii) methane gas was injected into the sample at room temperature and left for 3 days to complete its upward migration before cooling the system into the hydrate stability field.
2. Isolated pockets of gas or brine could exist in some pores. This can be due to gas reaching a pore that is not connected in the flow direction and/or capillary trapping. If such a pore is blocked in the flow direction, hydrate formation can trap the gas (Figure 4a). Similarly, hydrate formation in connected pores could also disconnect them, trapping brine/gas (Figure 4b). Capillary trapping can occur when the gas pressure is less than the capillary entry pressure of a given pore, which depends on its radius, resulting in the fluid being unable to move through that pore (Figure 4c). The formation of hydrate can enhance this trapping mechanism by decreasing the effective pore radius, resulting in higher threshold capillary pressures needed for gas invasion (Figure 4d).
3. Unconnected pores (occlusions) of gas/water can occur within hydrates (Figure 4e). In our experiment, the maximum hydrate and gas saturations are around 26% and 12% of the pore space, respectively. Near seafloor sediments on the southern summit of Hydrate Ridge (offshore Oregon, USA) contain porous hydrates that likely formed when methane gas bubbles became coated with a hydrate film as they moved upward within the sediments and coalesced together (Suess et al., 2001). A sufficiently thick hydrate film
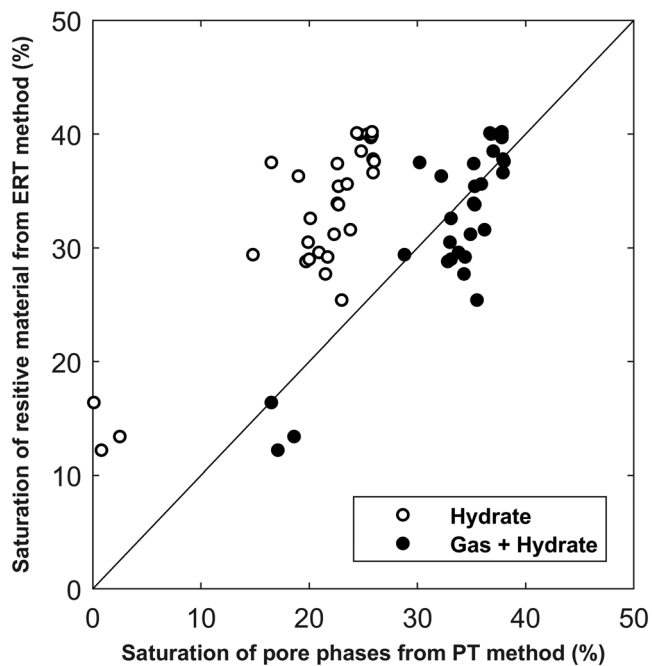
Figure 5. Total methane gas and methane hydrate saturations (volume percentage of pore space) from the pressure-temperature (PT) method plotted against saturation of all resistive material deduced from the resistivity (ERT) method. Relative errors in the saturations calculated from the ERT and PT methods are less than 2% and 0.5%, respectively.

enveloping the methane bubbles disconnects the gas remaining inside the hydrate film from the pore water outside (Figure 4f). Hence, gas remains trapped within the hydrate film, even though hydrate stability conditions prevail. Such porous hydrates have 55 ± 5% of their bulk volume filled with gas (Suess et al., 2001). Similar porous hydrate has also been recovered offshore Nigeria, with pore diameter of 2–3 mm (Sultan et al., 2014). We propose that this is the dominant mechanism for coexisting gas in our experimental setup. This mechanism does not involve three phase thermodynamic equilibrium, as the trapped methane gas inside the hydrate shell is not in physical contact with water outside the shell.

During drilling in a pockmark offshore Nigeria, Sultan et al. (2014) observed a vigorous flow of gas in the GHSZ, just after penetrating a thin hydrate layer at around 18 m below seafloor. These authors attributed this flow to rapid influx of gas along fractures in the GHSZ, which leads to rapid hydrate formation, primarily along the inner surface of fractures, leading to isolation of free gas from the surrounding pore fluid. This mechanism is similar to the one that we propose, but at much larger scale.

Gas trapped within hydrate films would diffuse out over geological time scales, so our experimental results might not reproduce well hydrate formation in nature. However, in a dynamic natural system with ongoing gas flow into the GHSZ, methane bubbles with a hydrate film enveloping them can also be present. Samples collected from the shallower sediments at Hydrate Ridge show that the residence time of such hydrate enveloped-methane bubbles may be less than the time needed for diffusion (Suess et al., 2001).

Further evidence for such gas trapping comes from a laboratory study of methane production by hydrate dissociation by heating that showed an abrupt peak in methane production rate, while the rate of water production remained almost constant (Tang et al., 2005), perhaps due to release of coexisting methane gas. A similar abrupt peak in methane production has been observed also using depressurization (Xiong et al., 2012).

4.2. Effect of Coexisting Gas Within the GHSZ on Hydrate Saturation Estimates

Resistivity-based methods for determining hydrate saturation do not differentiate between gas and hydrate; all resistive material in the pore space within the GHSZ is generally interpreted as hydrate (e.g., Hsu et al., 2014; Schwalenberg et al., 2010; Weitemeyer et al., 2006). Similarly, in our experiment, if we interpret all resistive material in the pore space as hydrate, the ERT method overestimates the hydrate saturation because both gas and hydrate are resistive compared to brine (Figure 5). Small apparent fluctuations in the total amount of resistive material inferred from ERT results come from uncertainty when selecting the empirical parameters in equation (17) (section 3.2). The PT method can differentiate between methane gas and hydrate because gas and hydrate have different volumetric densities (section 3.1). In our laboratory experiment, up to 36% of the resistive material remained as gas. In a borehole offshore Japan, the difference between hydrate saturation from resistivity methods and from sonic methods was ~50%, likely due to coexisting gas (Miyakawa et al., 2014). Table 1 lists other field studies with differences in hydrate saturation inferred from resistivity methods and seismic/sonic methods.

Further uncertainties in methane quantification based on resistivity data can occur due to such coexisting gas. The methane content per unit volume of the gas phase is different to that of the hydrate phase. The difference depends on the molar volumes of hydrate and gas, which in turn depend on pressure and temperature, with greater variations in the gas phase than in the hydrate phase. Hence, the uncertainty in the methane inventory is larger in shallower water depths where gas molar volumes are higher. The methane content of the GHSZ is overestimated in shallower waters (e.g., less than ~1,250 m depth for the Arctic Ocean) and underestimated in deeper waters, where the molar volume of methane gas is less than that of hydrate. If the amount of coexisting gas within the GHSZ is significant, then it can affect the estimate of carbon content, and the geophysical

and mechanical properties of the hydrate bearing sediments. Current numerical models that simulate the behavior of natural and laboratory hydrate systems do not account for this type of coexisting gas. Additional work is needed to support further our results, such as performing a similar study on different types of samples, and/or synchrotron X-ray computed tomography of hydrate- and gas-bearing samples.

5. Conclusions

In repeated cycles of hydrate formation and dissociation, our experimental results demonstrate the coexistence of up to 26% hydrate with about 12% gas. We infer that not all of the methane gas and water formed hydrate even when the two phase water-hydrate stability conditions were satisfied. We suggest that such coexistence occurs when methane gas bubbles become enveloped in hydrate films. A sufficiently thick hydrate film would isolate the gas trapped inside from the brine outside, even when hydrate stability conditions prevail. Such methane bubbles enveloped in hydrate films have also been observed in samples from Hydrate Ridge, offshore Oregon USA, with up to 55% of the bulk hydrate volume made up of coexisting gas. Our experimental results show that hydrate formation from methane in the gas phase results in up to 36% coexisting gas (as a percentage of the bulk hydrate volume).

Our results support the idea that coexisting gas may be present within the GHSZ in natural gas hydrate systems, with gas influx through fractures in fine-grained sediments. We suggest that this coexistence of gas and hydrate is one possible explanation for the differences in hydrate saturation estimates between resistivity and seismic/sonic observations of natural hydrate systems.

References

Archie, G. E. (1942). The electrical resistivity log as an aid in determining some reservoir characteristics. *Transactions of AIME*, *146*(01), 54–62. https://doi.org/10.2118/942054-G

Attias, E., Weitemeyer, K. A., Minshull, T. A., Best, A. I., Sinha, M., Jegen-Kulcsar, M., et al. (2016). Controlled-source electromagnetic and seismic delineation of subseafloor fluid flow structures in a gas hydrate province, offshore Norway. *Geophysical Journal International*, *206*(2), 1093–1110. https://doi.org/10.1093/gji/ggw188

Bussian, A. E. (1983). Electrical conductance in a porous medium. *Geophysics*, *48*(9), 1258–1268. https://doi.org/10.1190/1.1441549

Chaouachi, M., Falenty, A., Sell, K., Enzmann, F., Kersten, M., Haberthür, D., & Kuhs, W. F. (2015). Microstructural evolution of gas hydrates in sedimentary matrices observed with synchrotron X-ray computed tomographic microscopy. *Geochemistry, Geophysics, Geosystems*, *16*, 1711–1722. https://doi.org/10.1002/2015GC005811

Chen, M. P., Riedel, M., Spence, G. D., & Hyndman, R. D. (2008). Data report: A downhole electrical resistivity study of northern Cascadia marine gas hydrate. *Proceedings of the Integrated Drilling Program*, *311*. https://doi.org/10.2204/iodp.proc.311.203.2008

Clavier, C., Coates, G., & Dumanoir, J. (1984). Theoretical and experimental bases for the dual-water model for interpretation of Shaly Sands. *Society of Petroleum Engineers Journal*, *24*(02), 153–168. https://doi.org/10.2118/6859-PA

Clennell, M. B., Hovland, M., Booth, J. S., Henry, P., & Winters, W. J. (1999). Formation of natural gas hydrates in marine sediments: 1. Conceptual model of gas hydrate growth conditioned by host sediment properties. *Journal of Geophysical Research*, *104*(B10), 22,985–23,003. https://doi.org/10.1029/1999JB900175

de Lima, O. A. L., & Sharma, M. M. (1990). A grain conductivity approach to shaly sandstones. *Geophysics*, *55*(10), 1347–1356. https://doi.org/10.1190/1.1442782

Ellis, D. V., & Singer, J. M. (2007). Well logging for Earth scientists. In D. V. Ellis & J. M. Singer (Eds.). Dordrecht, Netherlands: Springer. https://doi.org/10.1007/978-1-4020-4602-5

Ellis, M. H. (2008). Joint seismic and electrical measurements of gas hydrates in continental margin sediments (PhD thesis), University of Southampton. Retrieved from http://eprints.soton.ac.uk/id/eprint/63293

Everett, D. H. (1961). The thermodynamics of frost damage to porous solids. *Transactions of the Faraday Society*, *57*, 1541. https://doi.org/10.1039/tf9615701541

Fohrmann, M., & Pecher, I. A. (2012). Analysing sand-dominated channel systems for potential gas-hydrate-reservoirs using an AVO seismic inversion technique on the southern Hikurangi margin, New Zealand. *Marine and Petroleum Geology*, *38*(1), 19–34. https://doi.org/10.1016/j.marpetgeo.2012.08.001

Fu, X., Porter, M., Viswanathan, H., Carey, J., & Juanes, R. (2017). Controlled depressurization of a hydrate-crusted gas bubble: Insights from 2D experiments and phase-field modeling. In *The 9th International Conference on Gas Hydrates*. Denver. Retrieved from http://icgh9.csmspace.com/docs/ICGH9_FinalProgram.pdf?062017

Fujii, T., Suzuki, K., Takayama, T., Tamaki, M., Komatsu, Y., Konno, Y., et al. (2015). Geological setting and characterization of a methane hydrate reservoir distributed at the first offshore production test site on the Daini-Atsumi knoll in the eastern Nankai trough, Japan. *Marine and Petroleum Geology*, *66*, 310–322. https://doi.org/10.1016/j.marpetgeo.2015.02.037

Glover, P. W. J. (2010). A generalized Archie's law for n phases. *Geophysics*, *75*(6), E247–E265. https://doi.org/10.1190/1.3509781

Glover, P. W. J., Meredith, P. G., Sammonds, P. R., & Murrell, S. A. F. (1994). Ionic surface electrical conductivity in sandstone. *Journal of Geophysical Research*, *99*(B11), 21,635–21,650. https://doi.org/10.1029/94JB01474

Gorman, A. R., Holbrook, W. S., Hornbach, M. J., Hackwith, K. L., Lizarralde, D., & Pecher, I. (2002). Migration of methane gas through the hydrate stability zone in a low-flux hydrate province. *Geology*, *30*(4), 327. https://doi.org/10.1130/0091-7613(2002)030%3C0327:MOMGTT%3E2.0.CO;2

Goswami, B. K., Weitemeyer, K. A., Minshull, T. A., Sinha, M. C., Westbrook, G. K., Chabert, A., et al. (2015). A joint electromagnetic and seismic study of an active pockmark within the hydrate stability field at the Vestnesa ridge, West Svalbard margin. *Journal of Geophysical Research: Solid Earth*, *120*, 6797–6822. https://doi.org/10.1002/2015JB012344

Guerin, G., Goldberg, D., & Meltser, A. (1999). Characterization of in situ elastic properties of gas hydrate-bearing sediments on the Blake ridge. *Journal of Geophysical Research*, *104*(B8), 17,781–17,795. https://doi.org/10.1029/1999JB900127

Han, T., Best, A. I., Sothcott, J., & Macgregor, L. M. (2011). Pressure effects on the joint elastic-electrical properties of reservoir sandstones. *Geophysical Prospecting*, *59*(3), 506–517. https://doi.org/10.1111/j.1365-2478.2010.00939.x

Han, T., Best, A. I., Sothcott, J., North, L. J., & MacGregor, L. M. (2015). Relationships among low frequency (2 Hz) electrical resistivity, porosity, clay content and permeability in reservoir sandstones. *Journal of Applied Geophysics*, *112*, 279–289. https://doi.org/10.1016/j.jappgeo.2014.12.006

Handa, Y. P., & Stupin, D. (1992). Thermodynamic properties and dissociation characteristics of methane and propane hydrates in 70-angstrom-radius silica-gel pores. *Journal of Physical Chemistry*, *96*(21), 8599–8603. https://doi.org/10.1021/j100200a071

Henry, P., Thomas, M., & Clennell, M. B. (1999). Formation of natural gas hydrates in marine sediments: 2. Thermodynamic calculations of stability conditions in porous sediments. *Journal of Geophysical Research*, *104*(B10), 23,005–23,022. https://doi.org/10.1029/1999JB900167

Hesse, R., & Harrison, W. E. (1981). Gas hydrates (clathrates) causing pore-water freshening and oxygen isotope fractionation in deep-water sedimentary sections of terrigenous continental margins. *Earth and Planetary Science Letters*, *55*(3), 453–462. https://doi.org/10.1016/0012-821X(81)90172-2

Hsu, S. K., Chiang, C. W., Evans, R. L., Chen, C. S., Chiu, S. D., Ma, Y. F., et al. (2014). Marine controlled source electromagnetic method used for the gas hydrate investigation in the offshore area of SW Taiwan. *Journal of Asian Earth Sciences*, *92*, 224–232. https://doi.org/10.1016/j.jseaes.2013.12.001

Hustoft, S., Bünz, S., Mienert, J., & Chand, S. (2009). Gas hydrate reservoir and active methane-venting province in sediments on <20 ma young oceanic crust in the Fram Strait, offshore NW-Svalbard. *Earth and Planetary Science Letters*, *284*(1–2), 12–24. https://doi.org/10.1016/j.epsl.2009.03.038

Hwang, M. J., Wright, D. A., Kapur, A., & Holder, G. D. (1990). An experimental study of crystallization and crystal growth of methane hydrates from melting ice. *Journal of Inclusion Phenomena and Molecular Recognition in Chemistry*, *8*(1–2), 103–116. https://doi.org/10.1007/BF01131291

Jackson, P. D., Smith, D. T., & Stanford, P. N. (1978). Resistivity-porosity-particle shape relationships for marine sands. *Geophysics*, *43*(6), 1250–1268. https://doi.org/10.1190/1.1440891

Kan, R., & Sen, P. N. (1987). Electrolytic conduction in periodic arrays of insulators with charges. *The Journal of Chemical Physics*, *86*(10), 5748–5756. https://doi.org/10.1063/1.452502

Kvenvolden, K. A. (1993). Gas hydrates—Geological perspective and global change. *Reviews of Geophysics*, *31*(2), 173–187. https://doi.org/10.1029/93RG00268

Lee, M. W., & Collett, T. S. (2006a). Gas hydrate and free gas saturations estimated from velocity logs on Hydrate Ridge, offshore Oregon, U.S. A. In *Proceedings of the Ocean Drilling Program, 199 scientific results* (Vol. 204, pp. 1–25). College Station, TX: Ocean Drilling Program. https://doi.org/10.2973/odp.proc.sr.204.103.2006

Lee, M. W., & Collett, T. S. (2006b). A method of Shaly sand correction for estimating gas hydrate saturations using downhole electrical resistivity log data. U.S. Geological Survey Scientific Investigations Report, 1–10. Retrieved from https://pubs.usgs.gov/sir/2006/5121/pdf/sir5121_508.pdf

Lee, M. W., & Collett, T. S. (2008). Integrated analysis of well logs and seismic data to estimate gas hydrate concentrations at Keathley canyon, Gulf of Mexico. *Marine and Petroleum Geology*, *25*(9), 924–931. https://doi.org/10.1016/j.marpetgeo.2007.09.002

Liu, X., & Flemings, P. B. (2006). Passing gas through the hydrate stability zone at southern hydrate ridge, offshore Oregon. *Earth and Planetary Science Letters*, *241*(1–2), 211–226. https://doi.org/10.1016/j.epsl.2005.10.026

Lu, Z., & Sultan, N. (2008). Empirical expressions for gas hydrate stability law, its volume fraction and mass-density at temperatures 273.15 K to 290.15 K. *Geochemical Journal*, *42*(2), 163–175. Retrieved from http://archimer.ifremer.fr/doc/00000/4958/. https://doi.org/10.2343/geochemj.42.163

Mavko, G. M., Mukerji, T., & Dvorkin, J (1998). *The rock physics handbook. Tools for seismic analysis in porous Media*. x + 329 pp. Cambridge, New York, Melbourne: Cambridge Univ. Press. Price £40.00, US $64.95 (hard covers)

McCleskey, R. B., Nordstrom, D. K., & Ryan, J. N. (2012). Comparison of electrical conductivity calculation methods for natural waters. *Limnology and Oceanography: Methods*, *10*(11), 952–967. https://doi.org/10.4319/lom.2012.10.952

Milkov, A. V., Dickens, G. R., Claypool, G. E., Lee, Y. J., Borowski, W. S., Torres, M. E., et al. (2004). Co-existence of gas hydrate, free gas, and brine within the regional gas hydrate stability zone at hydrate ridge (Oregon margin): Evidence from prolonged degassing of a pressurized core. *Earth and Planetary Science Letters*, *222*(3–4), 829–843. https://doi.org/10.1016/j.epsl.2004.03.028

Millero, F. J., Chen, C.-T., Bradshaw, A., & Schleicher, K. (1980). A new high pressure equation of state for seawater. *Deep Sea Research Part A. Oceanographic Research Papers*, *27*(3–4), 255–264. https://doi.org/10.1016/0198-0149(80)90016-3

Miyakawa, A., Saito, S., Yamada, Y., Tomaru, H., Kinoshita, M., & Tsuji, T. (2014). Gas hydrate saturation at site C0002, IODP expeditions 314 and 315, in the Kumano Basin, Nankai trough. *Island Arc*, *23*(2), 142–156. https://doi.org/10.1111/iar.12064

North, L. J., Best, A. I., Sothcott, J., & MacGregor, L. (2013). Laboratory determination of the full electrical resistivity tensor of heterogeneous carbonate rocks at elevated pressures. *Geophysical Prospecting*, *61*(2), 458–470. https://doi.org/10.1111/j.1365-2478.2012.01113.x

Peng, D.-Y., & Robinson, D. B. (1976). A new two-constant equation of state. *Industrial and Engineering Chemistry Fundamentals*, *15*(1), 59–64. https://doi.org/10.1021/i160057a011

Plaza-Faverola, A., Westbrook, G. K., Ker, S., Exley, R. J. K., Gailler, A., Minshull, T. A., & Broto, K. (2010). Evidence from three-dimensional seismic tomography for a substantial accumulation of gas hydrate in a fluid-escape chimney in the Nyegga pockmark field, offshore Norway. *Journal of Geophysical Research*, *115*, B08104. https://doi.org/10.1029/2009JB007078

Priest, J. A., Rees, E. V. L., & Clayton, C. R. I. (2009). Influence of gas hydrate morphology on the seismic velocities of sands. *Journal of Geophysical Research*, *114*, B11205. https://doi.org/10.1029/2009JB006284

Revil, A., Cathles, L. M., Losh, S., & Nunn, J. A. (1998). Electrical conductivity in shaly sands with geophysical applications. *Journal of Geophysical Research*, *103*(B10), 23,925–23,936. https://doi.org/10.1029/98JB02125

Revil, A., & Glover, P. W. J. (1998). Nature of surface electrical conductivity in natural sands, sandstones, and clays. *Geophysical Research Letters*, *25*(5), 691–694. https://doi.org/10.1029/98GL00296

Riestenberg, D., West, O., Lee, S., McCallum, S., & Phelps, T. J. (2003). Sediment surface effects on methane hydrate formation and dissociation. *Marine Geology*, *198*(1–2), 181–190. https://doi.org/10.1016/S0025-3227(03)00100-2

Rutter, E. H., & Glover, C. T. (2012). The deformation of porous sandstones; are Byerlee friction and the critical state line equivalent? *Journal of Structural Geology*, *44*, 129–140. https://doi.org/10.1016/j.jsg.2012.08.014

Schicks, J. M., Naumann, R., Erzinger, J., Hester, K. C., Koh, C. A., & Sloan, E. D. (2006). Phase transitions in mixed gas hydrates: Experimental observations versus calculated data. *Journal of Physical Chemistry B*, *110*(23), 11,468–11,474. https://doi.org/10.1021/jp0612580

Schnurle, P., Liu, C.-S., Hsiuan, T.-H., & Wang, T.-K. (2004). Characteristics of gas hydrate and free gas offshore southwestern Taiwan from a combined MCS/OBS data analysis. *Marine Geophysical Researches*, *25*(1–2), 157–180. https://doi.org/10.1007/s11001-005-0740-6

Schwalenberg, K., Haeckel, M., Poort, J., & Jegen, M. (2010). Evaluation of gas hydrate deposits in an active seep area using marine controlled source electromagnetics: Results from Opouawe Bank, Hikurangi margin, New Zealand. *Marine Geology*, *272*(1–4), 79–88. https://doi.org/10.1016/j.margeo.2009.07.006

Simandoux, P. (1963). Dielectric measurements in porous media and application to shaly formations. *Revue de l'Institut Francais du Petrole*, *18*(Suppl. issue), 193–215.

Skinner, B. J. (1966). Thermal expansion. In J. Clark, & P. Sydney (Eds.), *Handbook of physical constants* (pp. 75–96). America: Geological Society. https://doi.org/10.1130/MEM97-p75

Sloan, E. D., & Koh, C. A. (2007). *Clathrate hydrates of natural gases*. New York: CRC Press. Retrieved from https://www.crcpress.com/Clathrate-Hydrates-of-Natural-Gases-Third-Edition/Sloan-Jr-Koh/p/book/9780849390784. https://doi.org/10.1201/9781420008494

Smith, A. J., Flemings, P. B., Liu, X., & Darnell, K. (2014). The evolution of methane vents that pierce the hydrate stability zone in the world's oceans. *Journal of Geophysical Research: Solid Earth*, *119*, 6337–6356. https://doi.org/10.1002/2013JB010686

Spangenberg, E. (2001). Modeling of the influence of gas hydrate content on the electrical properties of porous sediments. *Journal of Geophysical Research*, *106*(B4), 6535–6548. https://doi.org/10.1029/2000JB900434

Suess, E., Torres, M. E., Bohrmann, G., Collier, R. W., Rickert, D., Goldfinger, C., et al. (2001). Sea floor methane hydrates at hydrate ridge, Cascadia margin. In *Natural gas hydrates—Occurrence, distribution and detection* (pp. 87–98). Washington, DC: American Geophysical Union. https://doi.org/10.1029/GM124p0087

Sultan, N., Bohrmann, G., Ruffine, L., Pape, T., Riboulot, V., Colliat, J. L., et al. (2014). Pockmark formation and evolution in deep water Nigeria: Rapid hydrate growth versus slow hydrate dissolution. *Journal of Geophysical Research:Solid Earth*, *119*, 2679–2694. https://doi.org/10.1029/2010JB007453

Sultaniya, A. K., Priest, J. A., & Clayton, C. R. I. (2015). Measurements of the changing wave velocities of sand during the formation and dissociation of disseminated methane hydrate. *Journal of Geophysical Research: Solid Earth*, *120*, 778–789. https://doi.org/10.1002/2014JB011386

Sun, R., & Duan, Z. (2007). An accurate model to predict the thermodynamic stability of methane hydrate and methane solubility in marine environments. *Chemical Geology*, *244*(1–2), 248–262. https://doi.org/10.1016/j.chemgeo.2007.06.021

Tang, L. G., Xiao, R., Huang, C., Feng, Z. P., & Fan, S. S. (2005). Experimental investigation of production behavior of gas hydrate under thermal stimulation in unconsolidated sediment. *Energy and Fuels*, *19*(6), 2402–2407. https://doi.org/10.1021/ef050223g

Thomas, E. C. (1976). The determination of qv from membrane potential measurements on Shaly Sands. *Journal of Petroleum Technology*, *28*(09), 1087–1096. https://doi.org/10.2118/5505-PA

Tishchenko, P., Hensen, C., Wallmann, K., & Wong, C. S. (2005). Calculation of the stability and solubility of methane hydrate in seawater. *Chemical Geology*, *219*(1–4), 37–52. https://doi.org/10.1016/j.chemgeo.2005.02.008

Tohidi, B., Danesh, A., & Todd, A. C. (1995). Modelling single and mixed electrolyte solutions and its applications to gas hydrates. *Chemical Engineering Research and Design*, *73*(A4), 464–472. Retrieved from http://www.scopus.com/inward/record.url?eid=2-s2.0-0029301853&partnerID=tZOtx3y1

Torres, M. E., Wallmann, K., Tréhu, A. M., Bohrmann, G., Borowski, W. S., & Tomaru, H. (2004). Gas hydrate growth, methane transport, and chloride enrichment at the southern summit of hydrate ridge, Cascadia margin off Oregon. *Earth and Planetary Science Letters*, *226*(1–2), 225–241. https://doi.org/10.1016/j.epsl.2004.07.029

Uchida, T., Takeya, S., Chuvilin, E. M., Ohmura, R., Nagao, J., Yakushev, V. S., et al. (2004). Decomposition of methane hydrates in sand, sandstone, clays and glass beads. *Journal of Geophysical Research*, *109*, B05206. https://doi.org/10.1029/2003JB002771

Vafaei, M. T., Kvamme, B., Chejara, A., & Jemai, K. (2014). A new reservoir simulator for studying hydrate dynamics in reservoir. *International Journal of Greenhouse Gas Control*, *23*, 12–21. https://doi.org/10.1016/j.ijggc.2014.02.001

Waite, W. F., Winters, W. J., & Mason, D. H. (2004). Methane hydrate formation in partially water-satulated Ottawa sand. *American Mineralogist*, *89*(8-9), 1202–1207. https://doi.org/10.2138/am-2004-8-906

Waxman, M. H., & Smits, L. J. M. (1968). Electrical conductivities in oil-bearing Shaly Sands. *Society of Petroleum Engineers Journal*, *8*(02), 107–122. https://doi.org/10.2118/1863-A

Weitemeyer, K. A., Constable, S. C., Key, K. W., & Behrens, J. P. (2006). First results from a marine controlled-source electromagnetic survey to detect gas hydrates offshore Oregon. *Geophysical Research Letters*, *33*, L03304. https://doi.org/10.1029/2005GL024896

White, R. S. (1977). Seismic bright spots in the Gulf of Oman. *Earth and Planetary Science Letters*, *37*(1), 29–37. https://doi.org/10.1016/0012-821X(77)90143-1

Winters, W. J., Pecher, I. A., Waite, W. F., & Mason, D. H. (2004). Physical properties and rock physics models of sediment containing natural and laboratory-formed methane gas hydrate. *American Mineralogist*, *89*, 1221–1227. https://doi.org/10.2138/am-2004-8-909

Xiong, L., Li, X., Wang, Y., & Xu, C. (2012). Experimental study on methane hydrate dissociation by depressurization in porous sediments. *Energies*, *5*(2), 518–530. https://doi.org/10.3390/en5020518

Yang, L., Falenty, A., Chaouachi, M., Haberthür, D., & Kuhs, W. F. (2016). Synchrotron X-ray computed microtomography study on gas hydrate decomposition in a sedimentary matrix. *Geochemistry, Geophysics, Geosystems*, *17*, 3717–3732. https://doi.org/10.1002/2016GC006521

You, K., Kneafsey, T. J., Flemings, P. B., Polito, P., & Bryant, S. L. (2015). Salinity-buffered methane hydrate formation and dissociation in gas-rich systems. *Journal of Geophysical Research: Solid Earth*, *120*, 643–661. https://doi.org/10.1002/2014JB011190

Zhan, X., Schwartz, L. M., Toksöz, M. N., Smith, W. C., & Morgan, F. D. (2010). Pore-scale modeling of electrical and fluid transport in Berea sandstone. *Geophysics*, *75*(5), F135–F142. https://doi.org/10.1190/1.3463704